

Filtering and Classification of Microcalcifications in Mammogram Images using Persistent Homology

Aminah Abdul Malek ^{1,2}, Mohd Almie Alias ^{2,3,*}, Fatimah Abdul Razak ^{2,3}, Mohd Salmi Md Noorani ², Rozi Mahmud ⁴, Nur Fariha Syaqina Zulkepli ⁵

¹ Mathematical Sciences Studies, College of Computing, Informatics and Media, Universiti Teknologi MARA (UiTM) Negeri Sembilan Branch, Seremban Campus, 70300 Seremban, Negeri Sembilan, Malaysia; aminah6869@uitm.edu.my

² Department of Mathematical Sciences, Faculty of Science & Technology, Universiti Kebangsaan Malaysia, UKM, Bangi 43600, Selangor, Malaysia

³ Centre for Modelling and Data Analysis (DELTA), Faculty of Science & Technology, Universiti Kebangsaan Malaysia, UKM, Bangi 43600, Selangor, Malaysia

⁴ Department of Radiology and Imaging, Faculty of Medicine and Health Sciences, University Putra Malaysia, 43400, Serdang, Selangor, Malaysia

⁵ School of Mathematical Sciences, Universiti Sains Malaysia, 11800 USM, Penang, Malaysia

* Correspondence: mohdalmie@ukm.edu.my

Simple Summary: The appearance of microcalcifications in mammogram images is an essential predictor for radiologists to detect early-stage breast cancer. This study aims to demonstrate the strength of Persistent Homology (PH) in noise filtering and feature extraction integrated with machine learning models in classifying microcalcifications into benign and malignant cases. The methods are implemented on two public mammography datasets: Mammographic Image Analysis Society (MIAS) and Digital Database for Screening Mammography (DDSM). We discovered that PH with machine learning techniques could improve classification accuracy, and this may be helpful for radiologists and clinicians in early diagnosis.

Abstract: Microcalcifications in mammogram images are primary indicators for detecting early stages of breast cancer. However, dense tissues and noise in the images make it challenging to classify the microcalcifications. Currently, preprocessing procedures such as noise removal techniques are implemented directly into the images, which may produce a blurry effect and loss of image details. This study proposed a new approach using Persistent Homology (PH) in which the filtering process is not performed directly on the image matrix but through the diagrams arising from PH. These diagrams will enable us to distinguish prominent characteristics of the image from noise. The filtered diagrams are then vectorised using PH features, persistent image and persistent entropy, and are embedded in machine learning models to discriminate between benign and malignant classes. This study reveals that using appropriate PH filtering level and features coupled with machine learning techniques can improve classification accuracy.

Keywords: topological data analysis; persistent homology; microcalcification; filtering; image processing

Citation: To be added by editorial staff during production.

Academic Editor: Firstname Last-name

Received: date

Revised: date

Accepted: date

Published: date



Copyright: © 2022 by the authors. Submitted for possible open access publication under the terms and conditions of the Creative Commons Attribution (CC BY) license (<https://creativecommons.org/licenses/by/4.0/>).

1. Introduction

Female breast cancers continue to record an increase in new cases and are reported as the most common incidence and mortality cancer worldwide, surpassing other types of cancer [1]. According to the World Health Organization (WHO), more than 2.3 million women were diagnosed with breast cancer globally in 2020, and 685,000 died from the

disease [2]. It means that, on average, a woman is diagnosed with breast cancer every 14 seconds. Preventive measures, including imaging screening, can potentially detect cancer at an early stage, which in turn, increases the patient's survival rate [3]. Among the numerous screening methods currently available for the detection of breast cancer, mammography has become the main and effective imaging method in increasing the rate of early-stage cancer detection [4,5].

One of the important signs in cancer detection on mammographic images is the presence of microcalcifications, which appear as small bright spots within an inhomogeneous background [6]. Figure 1 shows an example of benign and malignant microcalcifications on mammogram images taken from the MIAS database [7]. Note that the morphology of this microcalcification is a crucial predictor of its pathological nature, with large, round, and oval calcifications of uniform size exhibiting benign (non-cancerous) characteristics while smaller, non-uniform calcifications exhibit characteristics of malignant growth [8,9]. In clinical practice, it is difficult and time-consuming for radiologists to interpret and evaluate microcalcifications accurately. This is true especially when the microcalcifications appear in low contrast and are obscured by the background tissue of the images [10]. Human errors based on subjective evaluations may lead to unnecessary biopsy procedures, which can cause harm and anxiety for the patients [11].

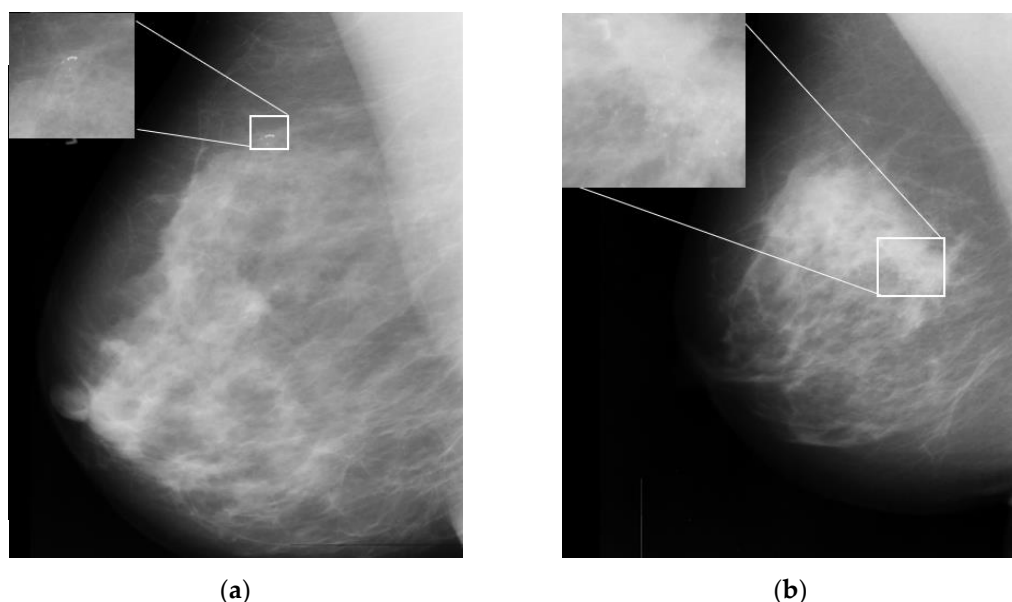


Figure 1. Sample microcalcification on mammogram images in MIAS dataset [7]. (a) benign microcalcifications; (b) malignant microcalcifications.

In order to improve the accuracy of assessing microcalcifications, numerous studies have been conducted to develop computational approaches that could potentially aid radiologists in distinguishing benign and malignant microcalcifications [5,12,13]. The standard computer-aided detection (CAD) processes consist of image preprocessing, segmentation, feature extraction, feature selection, and classification model, as depicted in Figure 2(a). Each phase involves a different technique, and the performance relies heavily on the preceding phase. Preprocessing is the initial phase of the image processing pipeline. Filtering is commonly used as preprocessing technique for removing noises and other artifacts in the image. Noise emerges in mammograms when the image's brightness varies in areas representing the same tissues due to non-uniform photon distribution [3]. It gives a grainy appearance which can reduce the visibility of some features within the image, especially microcalcifications in dense breast tissue. Since noise, edge, and texture are high-frequency components, distinguishing them is challenging [14].

Various filtering techniques have been used in the literature to reduce noise in mammogram images. Each method has its benefits and drawbacks. For example, Wiener filter is considered a linear filter that can improve the images by reducing random noise but may produce a blurry effect and incomplete noise filtration [15]. Non-linear filters, such as the median filter, can be utilised to overcome linear filter limitations since it has several benefits, such as being straightforward and offering a sensible noise removal performance, but they could distort fine edges even at low noise densities [16]. The comparative reviews from [14,17,18] agreed that different types of noise require different filtering techniques.

Another important phase that influences classification performance is feature extraction [11]. Feature extraction methodologies analyse images to extract the most prevalent features and are employed as inputs to machine learning classifiers to distinguish between benign and malignant classes. Such features included intensity, statistical, shape, and textural. The most common feature used in mammogram classification is texture features [5]. The gray-level cooccurrence matrix (GLCM), which calculates the occurrence of various grey levels in a region of interest (ROI), is a well-known texture feature proposed by [22] and utilised extensively in the literature [13,16,19,20]. Nevertheless, all these features focus on local information of the images and are often burdened with details, resulting in data complexity [21].

This study proposes a new classification approach based on the Persistent Homology (PH) that can extract informative features from the images, which consists of the filtering and feature extraction processes, as shown in Figure 2(b).

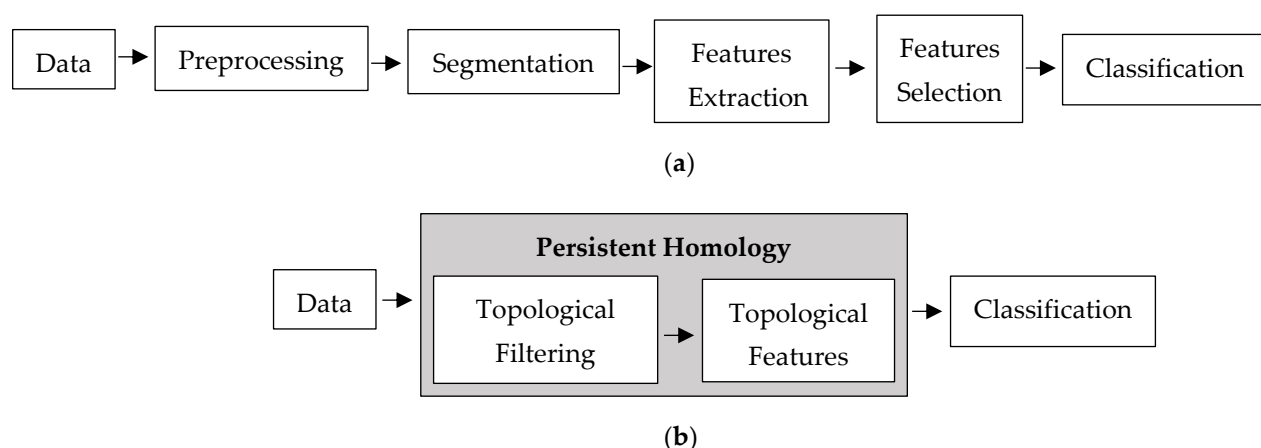


Figure 2. Computer-aided detection processes. (a) Standard processes; (b) Proposed techniques

PH, the core tool of topological data analysis (TDA), has been widely employed in recent years as a multi-scale representation of topological features. It can extract topological summaries from data that capture the birth and death of connected components, loops, and voids through a filtration process [21–26]. Apart from that, Persistence diagrams (PD) are one of the topological descriptors produced by the PH [27]. It comprises a collection of points in the half-plane above the diagonal with coordinates (birth, death) of topological features, helpful in distinguishing robust and noisy topological properties [28]. The geometric measurement of the associated topological properties directly correlates with the lifespan (differences between death and birth), where the long lifespan is considered a prominent feature represented by the points far from the diagonal in the diagram. In contrast, the short lifespans representing points close to the diagonal are interpreted as noise [21,29,30].

There has been minimal effort to explore the potential use of persistent diagrams as a filtering approach, especially in mammogram images. A noteworthy study by [31] filtered out 20% of points close to the diagonal in PD, but they focused on interpreting

quality assessment in the eye fundus image. The persistent diagram of a microcalcifications image contains thousands of points with many short lifespans (noise), necessitating an additional filtering procedure. Thus, we propose a novel method for filtering noise in a persistent diagram based on the maximum lifespan of the image.

In PH, the topological features generated from PD can be vectorised and integrated into machine learning models. Various vectorisation approaches have been proposed, with promising results in various fields. For example, the Persistent Image (PI) feature proposed by [32] has been used in hepatic tumour classification with considerable accuracy [33,34], Persistent Entropy (PE) and p-norm features were used for dark soliton detection [35], and Persistent Landscapes (PL) in the quantitative analysis of fluorescence microscopy images [36]. Furthermore, [23] used Betti numbers for evaluating tumor heterogeneity in image feature extraction.

Nevertheless, a recent study by [37] stated that keeping track of the lifespan is more informative than the progression of Betti numbers. They used mean, the standard deviation of lifespan for each cycle, and persistent entropy for 0- and 1-dimension features to embed in machine learning techniques in detecting the correct Gleason score of prostate cancer, reporting an accuracy of above 95%. In other words, selecting suitable topological features is crucial since the suitability of features depends on the data type and the problem at hand.

In this study, we explored the potential use of Persistent Homology method for noise filtering and feature extraction processes. To the best of our knowledge, this is the first work using PH to tackle the challenge of filtering noise as well as selecting suitable topological features to improve the classification performance of microcalcifications in mammogram images. The purpose of this paper can be summarised as follows. (i) Filtering multi-level noise of 1-dimensional homology group PD based on maximum lifespan. (ii) Vectorise topological features from the PD using the persistent image and persistent entropy to discriminate between malignant and benign classes. (iii) Compare the performance of the filter and non-filter PD, as well as the performance of individual and concatenate vectorised features using several machine learning models. (iv) Suggest the optimal filtration level for MIAS and DDSM datasets. Since this work aims to highlight the importance of a topological approach to classifying the microcalcifications in a machine learning setting, prior knowledge of machine learning is assumed and will not be recalled in this section or elsewhere in the paper.

2. Materials and Methods

The proposed classification framework consists of four main steps: data acquisition, topological filtering, topological features vectorisation, and classification using machine learning classifiers, as illustrated in Figure 3.

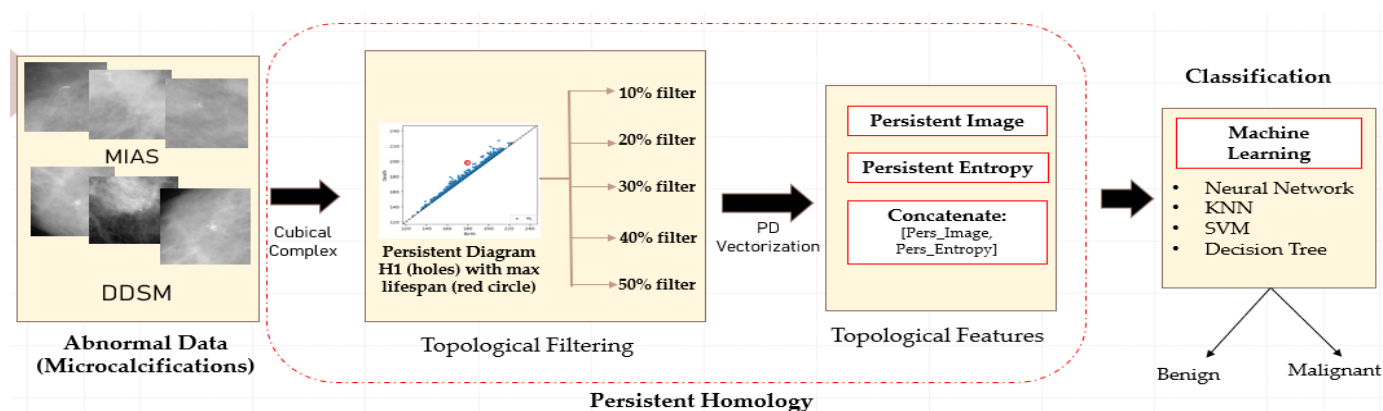


Figure 3. Illustration of the proposed classification framework using Persistent Homology.

2.1 Dataset

The data used in this study consist of two publicly available datasets whose region of interest contains microcalcifications. The first dataset was taken from the MIAS dataset [7], containing 26 image patches with a size of 200×200 pixels. There were thirteen malignant and benign cases each with three types of background tissue: fatty, fatty glandular and dense glandular. The second dataset was taken from the digital database for screening mammography (DDSM) dataset [38], consisting of 140 image patches randomly selected with seventy cases for malignant and benign each. The size of the images is set to 300×300 pixels. Despite a large number of mammograms in these two datasets, not all have microcalcification. Therefore, the number of microcalcification patches is substantially lower than the total number of images in the datasets.

2.2 Persistent Homology

Persistent Homology (PH) is a primary technique in TDA based on the concept that topological features detected over varying scales are more likely to represent intrinsic features [39,40]. Other than that, PH studies geometric patterns by looking at the evolution of k -dimensional holes such as 0-dimensional holes (H_0) representing connected components, 1-dimensional holes (H_1) representing loops, and 2-dimensional holes (H_2) voids.

Images can be interpreted as geometric shapes known as cubical complexes. In two-dimensional grayscale images, the cubical complexes are topological spaces consist a combination of 0-cube (vertices), 1-cube (edges), and 2-cube (squares). It can be efficiently constructed by assigning a vertex to each pixel, then combining vertices corresponding to nearby pixels by an edge and filling in the resulting squares [41]. Let I be a grayscale image of size $N \times M$ with grey intensities 2^n (we use 8-bit grayscale $n = 8$). The pixel intensity value of I on the intervals $[0, 2^n - 1]$ is $[0, 255]$ where 0 represents black colour, 255 for white colour, and shades of grey for the values in between. Once these images are interpreted as 2-cubical simplices, grayscale filtration with 256 sublevels can be constructed as a nested sequence $K_0 \subset K_1 \subset K_2 \subset \dots \subset K_{2^n-1}$ called sublevel set filtration [33]; see the example in Figure 4.

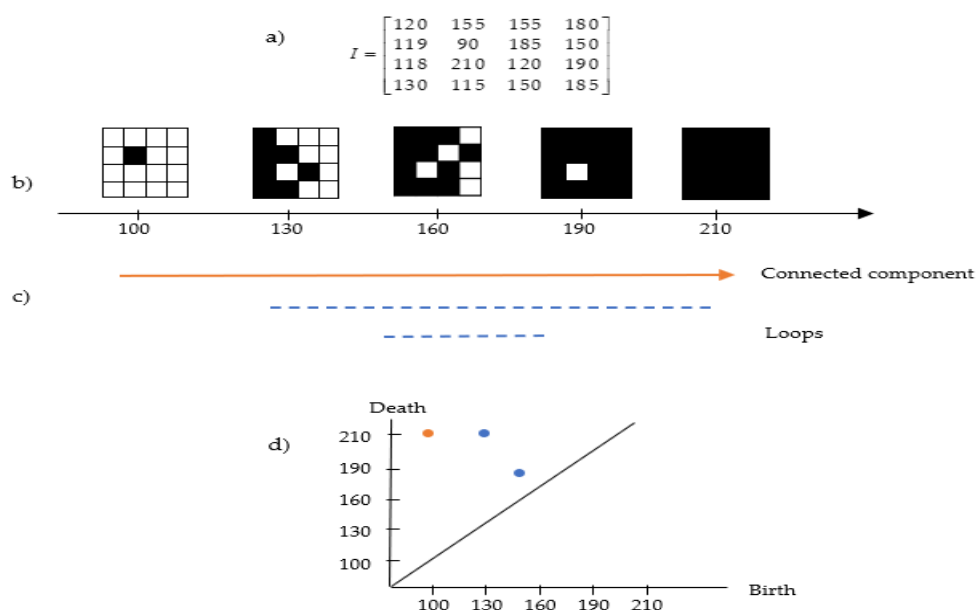


Figure 4. Example of the cubical complex in a grayscale image. (a) Image pixel values; (b) the filtered cubical complex; (c) the lifespan of connected components and loops based on (b); (d) the persistent diagram based on (c).

Figures 4 (a) and (b) present an example of cubical complex filtration in a matrix representing the pixel value of the image. The lifespan can be seen in Figure 4(c), where the connected component appears at the intensity of 100 and continues to exist because all subsequent pixels are always connected to the preceding ones. At filtration 120, a loop exists (full white pixels inside components made of black pixels) and deaths at filtration 210. Apart from that, another loop exists at filtration 150 and deaths shortly at filtration 185. This information can be transformed in the persistent diagram representation as in Figure 4(d), which will be discussed in the following section.

2.2.1 Interpreting the Persistent Diagrams

Persistence diagrams represent a pattern-generating field and provide a (visual) summary of the set of points $\{(b, d) \mid b, d \in \mathbb{R}^2\}$ and $d > b$, where the births (b) are marked on the x-axis and deaths (d) on the y-axis. The lifespan $d-b>0$ indicates the prominence of features. Long-lived features are allocated far from the diagonal line and are usually regarded as significant features and represent the robustness of holes against noise, whereas short lifespans represent points close to the diagonal and are interpreted as noise [33,42]. All points of the different homological dimensions are present in PD such as 0-dimensional holes denoted as H_0 (connected complete black pixels) and 1-dimensional holes denoted as H_1 or loops (complete white pixels inside components made of black pixels). However, some dimensions may be irrelevant to the study [22]. Since microcalcifications appear as white spots, this study employs only 1-dimensional holes (H_1). Figure 5 illustrates samples of PD for H_1 obtained from benign and malignant microcalcifications in different datasets.

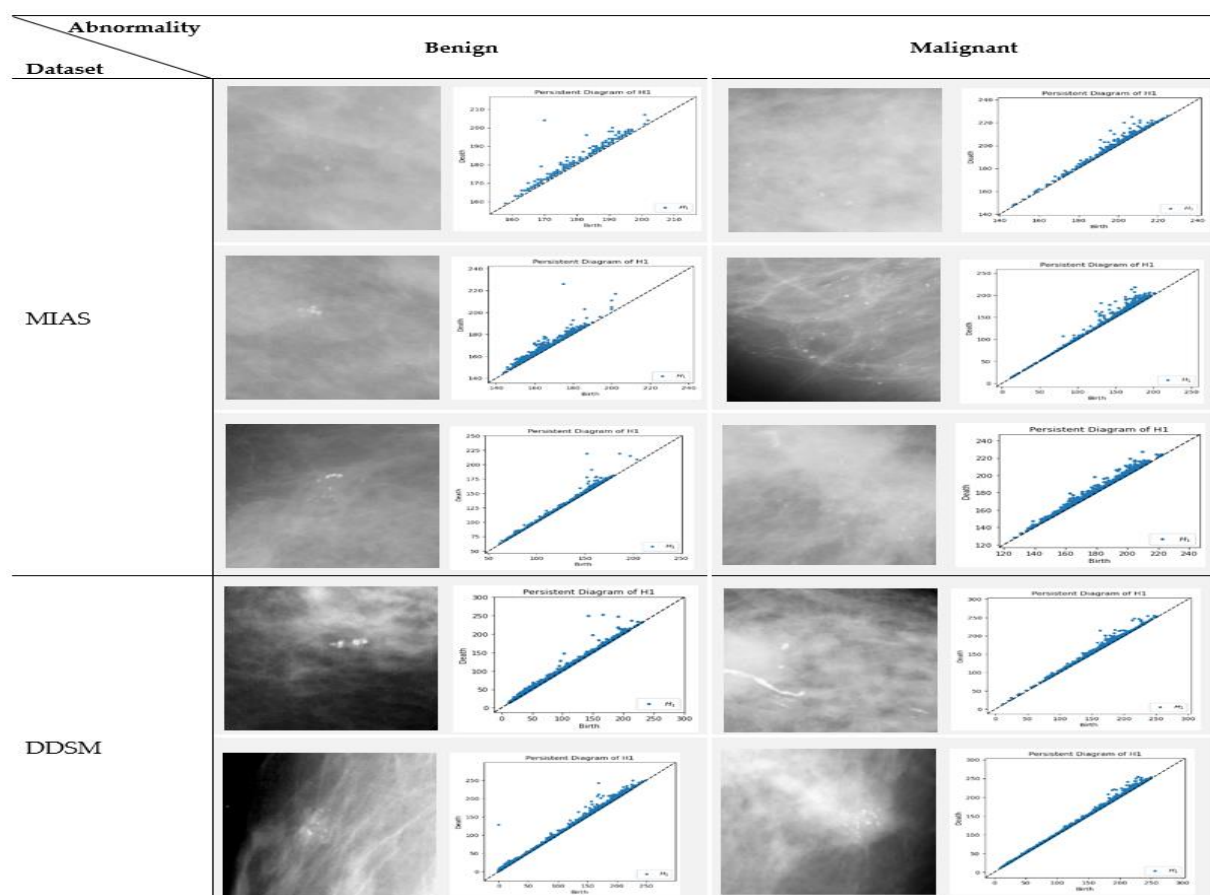


Figure 5. Persistent diagram of H_1 (loops) for benign and malignant microcalcifications in MIAS and DDSM datasets. For MIAS dataset, the first row is a sample of dense glandular tissue, the second row is a sample of fatty tissue, and the third row is fatty glandular tissue.

Similarly shaped will have comparable PD [43]. For example, based on Figure 5, the benign microcalcifications indicate a similar pattern for different types of density and datasets where the topological features associated with long-lived lifespan are seen. Conversely, for malignant microcalcifications, the PD illustrates short-lived features where the points are tightly packed and close to the diagonal. It is known that the points close to the diagonal line are usually regarded as less "useful" and linked with noise [44,45]. Thus, multi-level filtering of PD offers a rigorous solution to the problem of distinguishing between anomalies and noise in these representations. The proposed procedures are described in the following steps:

Step 1: Obtain PD for 1-dimensional holes (H_1);

Step 2: Calculate the lifespan for each point in PD;

Step 3: Find the maximum lifespan;

Step 4: Filter;

Filter_10% = lifespan > (0.1*max_lifespan)

Filter_20% = lifespan > (0.2*max_lifespan)

Filter_30% = lifespan > (0.3*max_lifespan)

Filter_40% = lifespan > (0.4*max_lifespan)

Filter_50% = lifespan > (0.5*max_lifespan)

We choose the filter interval range from 10% to 50% with 10% increments to facilitate interpretation when determining which level yields the best classification results for each dataset. The number of points in PD can be reported as Betti numbers denoted as B_1 for H_1 ; hence the filtering process will reduce the number of B_1 values. Figure 6 demonstrates a schematic representation of multi-level filtering PD in a sample of a malignant image.

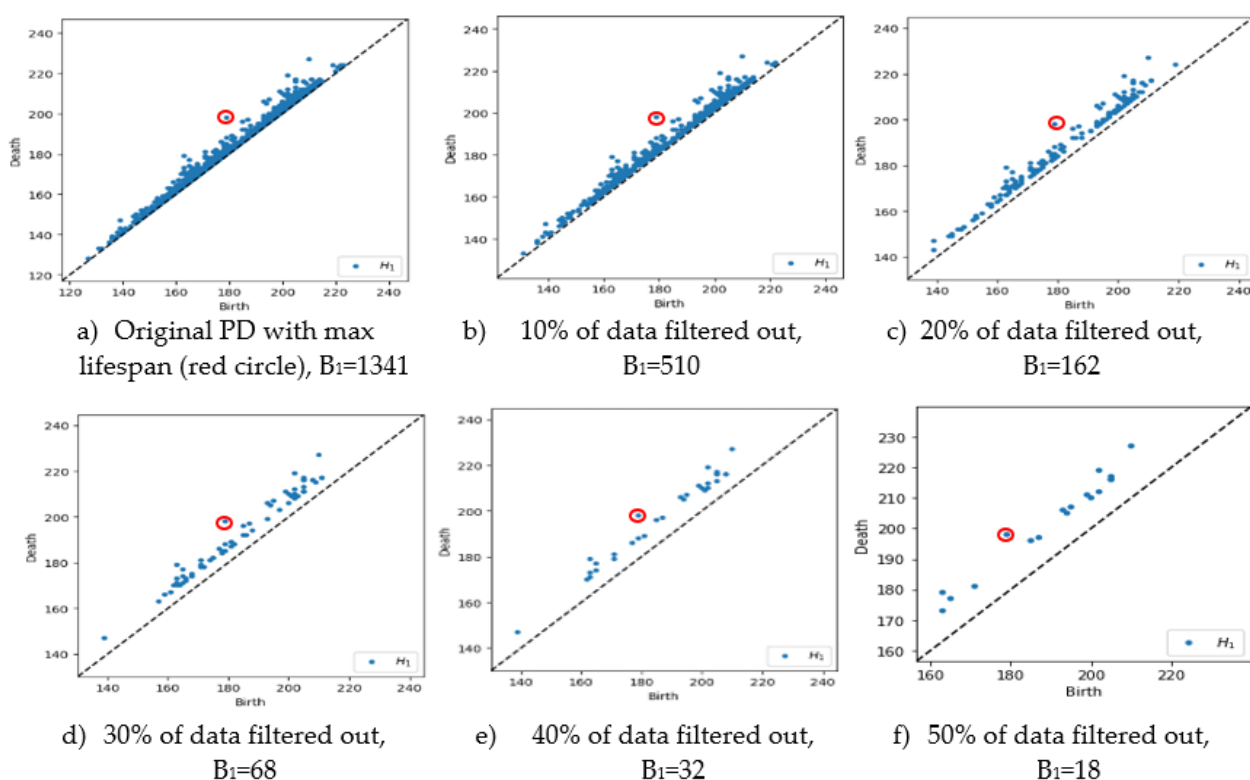


Figure 6. Example of multi-level filtering PD with Betti number (B_1)

Referring to Figure 6 (a), we calculate the lifespan for each point in the PD and obtain the maximum lifespan. In Figures 6(b) – 6(f), the points are filtered out based on a lifespan

greater than 10% to 50% of the maximum lifespan, which implies the number of B_1 reduced from 1341 points initially to 510, 162, 68, 32 and 18, respectively. The original and filtered PD is then used to obtain the feature vector representations, which can be easily incorporated as input in machine learning models.

2.2.2 Vectorised Topological Features

We employ two topological features to vectorise the persistence diagram so that the distribution of the persistence feature (lifespan) can be characterised between benign and malignant. The vectorised topological features used are described as follows.

- Persistent Entropy (PE)

PE measures the disorder in the distribution of lifespan (persistence). Let $PD = \{(b_j, d_j)\}_{j \in I}$ be a persistent diagram with b_j and d_j are the birth and death points of topological structure in pixel image I and lifespan $\ell = |d - b|$. The entropy of PD is defined by [31,46]:

$$\varepsilon(PD) = \sum_{j=1}^n \frac{\ell_j}{S(\ell_j)} \log \left(\frac{\ell_j}{S(\ell_j)} \right) \quad (1)$$

where $S(\ell_j)$ is the sum of the lifespan in the PD. Every PD will produce one entropy value. Based on [35], 0 entropy value represents a single feature in the image, while N features consist of $\varepsilon(PD) = \log(N)$.

- Persistent Image (PI)

PI is one of the prevalent vectorisation methods adopted to convert the topological information in PDs into a finite-dimensional vector representation. It has been introduced by Adams et al. [32]. To construct PI, the PD, which consists of the persistence point at birth(b)

– death(d) coordinates, is rotated by $\frac{\pi}{4}$. Then the rotated PD denoted as R can be discretised into the persistent surface (ρ) in (x, y) -coordinated defined as

$$\rho R(x, y) = \sum_{(b, d) \in R} g_{(b, d)}(x, y) \cdot f(b, d) \quad (2)$$

where $g_{(b, d)}$ is a gaussian smoothing function, $g_{(b, d)}(x, y) = \frac{1}{2\pi\sigma^2} e^{-[(x-b)^2 + (y-d)^2]/2\sigma^2}$ and $f(b, d) \geq 0$ are non-negative weighting functions [47]. Finally, the PI can be obtained by integrating the persistence surface function $\rho R(x, y)$ over each pixel. In our experiments, we choose pixel size = 1, meaning that we get one vectorise PI value for every PD. Other parameters, such as the weighting function, $f(b, d)$ is based on the persistence values [32] and the smoothing parameter in the gaussian function σ is set by default.

In all experiments, we extracted a 1-dimensional persistent diagram using an open source program, namely Cubical Ripser (https://github.com/shizuo-kaji/CubicalRipser_3dim/ accessed on 2 February 2022)[48], persistent image and persistent entropy feature using Scikit-TDA library written in python (<https://persim.scikit-tda.org/> accessed on 19 May 2022).

2.3. Machine Learning Classifier

Once the topological features are vectorised, the dataset is ready to be implemented in the machine learning classifier. We used the following models for comparison purposes:

- Neural Network (NN)
- Support Vector Machine (SVM)
- K-Nearest Neighbour (KNN)
- Decision Tree (DT)

For machine learning models, we performed in MATLAB R2021b using a classification learner with a five-fold cross-validation approach. All the classifier's parameters are at the default setting.

2.4 Performance Evaluation

Many different evaluation metrics can be used to measure how well the method and classifier work. This study uses the confusion matrix, accuracy, and area under the receiver operating characteristic curve (AUC). The metrics used to evaluate results are described below [49]:

- *Confusion matrix*: Provide a matrix as output that describes the method's performance consisting of the total number of correct and incorrect predictions. The matrix is shown in Figure 7.

		Prediction Class	
		Benign	Malignant
True Class	Benign	True Positives (TP)	False Negatives (FN)
	Malignant	False Positives (FP)	True Negatives (TN)

Figure 7. The confusion matrix

- *Classification Accuracy (CA)*: The percentage of microcalcifications correctly classified to the total number of observations. It can be measured as follow:

$$CA = \frac{TP + TN}{TP + TN + FP + FN} \quad (3)$$

- *The area under the curve (AUC)*: The AUC can be measured by calculating the area under the receiver operating characteristic (ROC) curve. The ROC curve is a plot of the true positive rate (TPR) or can also be called sensitivity or recall versus the false positive rate (FPR). TPR is defined in this context as the number of correctly diagnosed malignant cases divided by the total number of malignant cases. In contrast, s FPR is defined as the number of benign cases wrongly classified as malignant divided by the total number of benign instances. TPR and FPR can be calculated using equations (4) and (5), respectively:

$$TPR = \frac{TP}{TN + FN} \quad (4)$$

$$FPR = \frac{FP}{FP + TN} \quad (5)$$

3. Results

In this section, we present the results when the proposed method discussed in Section 2 was applied to two public datasets MIAS and DDSM. This section aims to discuss the usefulness of the Persistent homology approach in discriminating the topological features between two classes, benign and malignant. We also examine the performance of single and concatenate features using four machine learning classifiers by comparing the accuracy (CA) and area under the curve (AUC). Finally, the optimal topological filter for each dataset is also presented.

3.1 Topological Filtering

Figures 8 and 9 illustrate the scatter plot of persistent entropy versus a persistent image with different levels of topological filtering in MIAS and DDSM datasets, respectively.

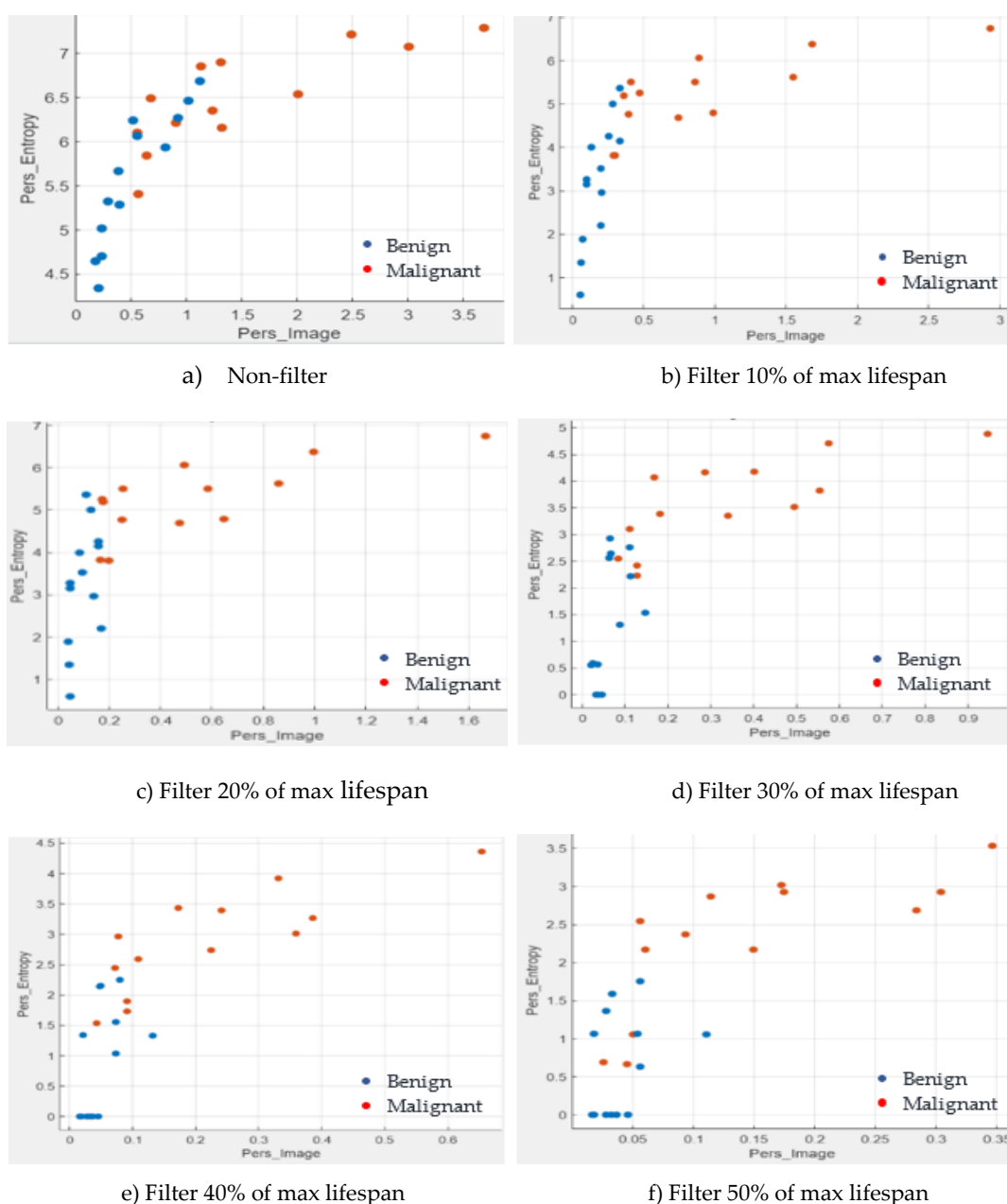


Figure 8. Scatter plot of persistent entropy versus a persistent image with different levels of filters in MIAS dataset

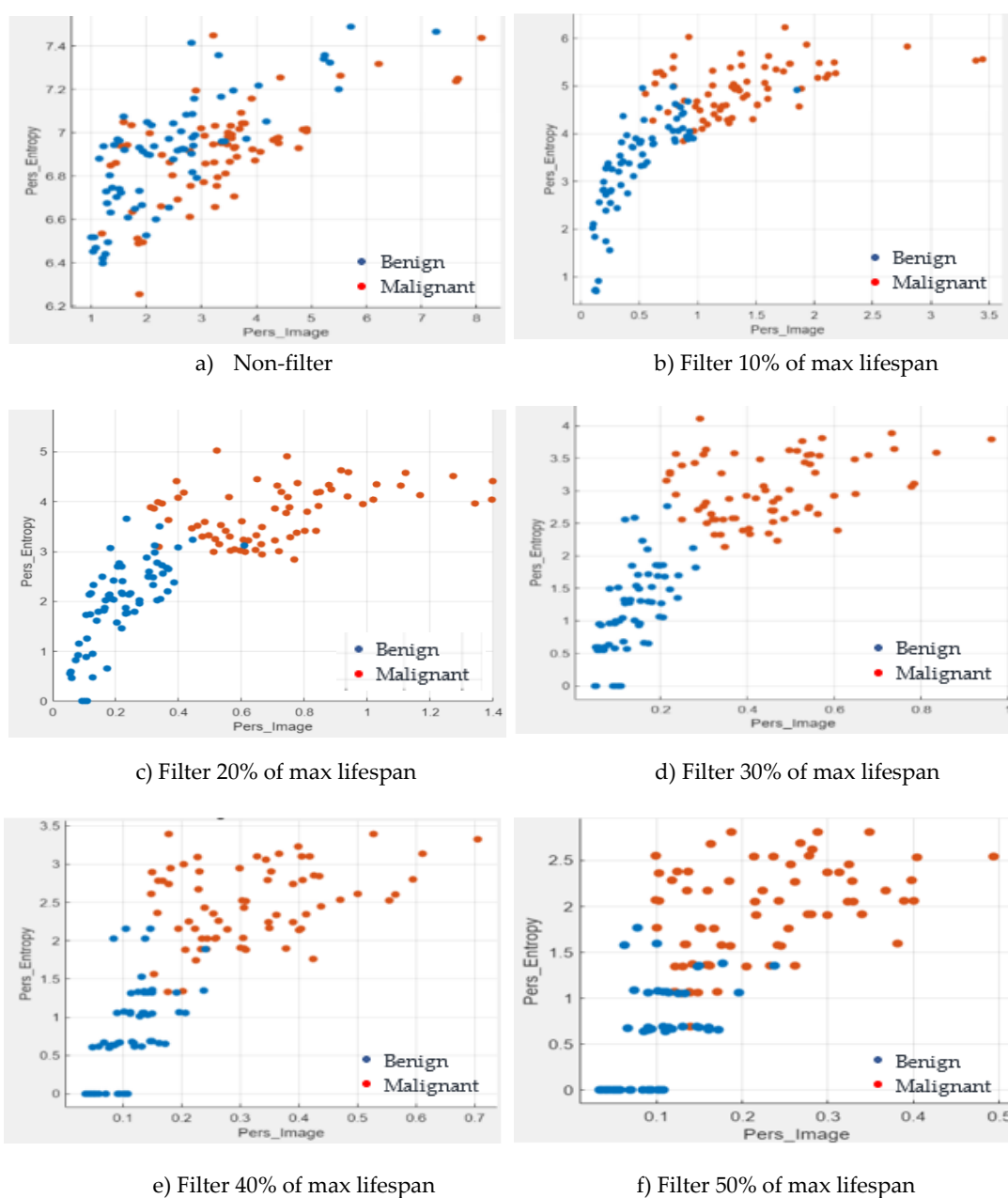


Figure 9. Scatter plot of persistent entropy versus a persistent image with different levels of filters in the DDSM dataset

Figures 8 and 9 demonstrate scatter plots where each point corresponds to the value of PE versus PI. The number of points represents 26 images in MIAS and 140 in DDSM datasets. It can be seen from the non-filtered PD in Figures 8(a) and 9(a), that the separation between two classes, benign and malignant, is more difficult to distinguish by the value of persistent entropy and persistent image features. Removing the short lifespan or noise through PD filtration in 10 to 30 percent gives a positive impact where the benign classes tend to have smaller values of persistent entropy and persistent image than the malignant class, as in Figures 8 and 9 (b-d). However, extremely high filters in PD (filter 40% and 50%) lead to overlapping in PE and PI values, as in Figures 6 and 7 (e-f).

3.2 Classification Performance

The optimum filtering level was selected by comparing the performance of the individual and concatenate topological features using four machine learning classifiers namely Neural Network (NN), K-Nearest Neighbors (KNN), Support Vector Machine (SVM), and Decision Tree (DT) models. Tables 1 and 2 present the performance of the persistence image feature, while Tables 3 and 4 are for the PE feature in MIAS and DDSM databases, respectively.

Table 1. Classification performance of PI feature in the MIAS dataset. CA = accuracy, Std = standard deviation.

Pers. Image Condition	NN		KNN		SVM		DT	
	CA \pm Std	AUC	CA \pm Std	AUC	CA \pm Std	AUC	CA \pm Std	AUC
Non-Filter	76.9 \pm 8.3	0.76	73.1 \pm 8.7	0.73	69.2 \pm 9.1	0.85	73.1 \pm 8.7	0.74
Filter 10%	80.8 \pm 7.7	0.91	73.1 \pm 8.7	0.73	73.1 \pm 8.7	0.86	73.1 \pm 8.7	0.74
Filter 20%	92.3 \pm 5.2	0.93	88.5 \pm 6.3	0.88	76.9 \pm 8.3	0.93	92.3 \pm 5.2	0.9
Filter 30%	76.9 \pm 8.3	0.89	76.9 \pm 8.3	0.77	73.1 \pm 8.7	0.89	73.1 \pm 8.7	0.74
Filter 40%	73.1 \pm 8.7	0.72	73.1 \pm 8.7	0.73	73.1 \pm 8.7	0.9	76.9 \pm 8.3	0.73
Filter 50%	69.2 \pm 9.1	0.69	69.2 \pm 9.1	0.69	73.1 \pm 8.7	0.85	73.1 \pm 8.7	0.68

Table 2. Classification performance of PI feature in the DDSM dataset

Pers. Image Condition	NN		KNN		SVM		DT	
	CA \pm Std	AUC	CA \pm Std	AUC	CA \pm Std	AUC	CA \pm Std	AUC
Non- Filter	71.4 \pm 3.8	0.74	50 \pm 4.2	0.5	59.3 \pm 4.2	0.69	63.6 \pm 4.1	0.68
Filter 10%	86.4 \pm 2.9	0.93	82.9 \pm 3.2	0.83	82.9 \pm 3.2	0.83	85.7 \pm 3	0.92
Filter 20%	90.7 \pm 2.5	0.95	86.4 \pm 2.9	0.86	92.9 \pm 2.2	0.94	90 \pm 2.5	0.93
Filter 30%	93.6 \pm 2.1	0.94	93.6 \pm 2.1	0.94	93.6 \pm 2.1	0.94	94.3 \pm 1.9	0.95
Filter 40%	91.4 \pm 2.4	0.97	87.1 \pm 2.8	0.87	89.3 \pm 2.6	0.97	87.1 \pm 2.8	0.85
Filter 50%	81.4 \pm 3.3	0.91	85 \pm 3	0.85	82.9 \pm 3.2	0.93	83.6 \pm 3.1	0.88

Table 3. Classification performance of PE feature in the MIAS dataset

Pers. Entropy Condition	NN		KNN		SVM		DT	
	CA \pm Std	AUC	CA \pm Std	AUC	CA \pm Std	AUC	CA \pm Std	AUC
Non-Filter	53.8 \pm 9.8	0.55	50 \pm 9.8	0.5	69.2 \pm 9.1	0.78	46.2 \pm 9.8	0.59
Filter 10%	57.7 \pm 9.7	0.7	65.4 \pm 9.3	0.65	65.4 \pm 9.3	0.79	65.4 \pm 9.3	0.69
Filter 20%	84.6 \pm 7.1	0.9	92.3 \pm 5.2	0.92	80.8 \pm 7.7	0.89	73.1 \pm 8.7	0.75
Filter 30%	80.8 \pm 7.7	0.83	80.8 \pm 7.7	0.81	80.8 \pm 7.7	0.89	80.8 \pm 7.7	0.8
Filter 40%	76.9 \pm 8.3	0.81	80.8 \pm 7.7	0.81	76.9 \pm 8.3	0.92	84.6 \pm 7.1	0.79
Filter 50%	76.9 \pm 8.3	0.79	73.1 \pm 8.7	0.73	80.8 \pm 7.7	0.89	88.5 \pm 6.3	0.83

Table 4. Classification performance of PE feature in the DDSM dataset

Pers. Entropy Condition	NN		KNN		SVM		Decision Tree	
	CA \pm Std	AUC	CA \pm Std	AUC	CA \pm Std	AUC	CA \pm Std	AUC
Non-Filter	50.7 \pm 4.2	0.55	50 \pm 4.2	0.5	49.3 \pm 4.2	0.53	55.7 \pm 4.2	0.54
Filter 10%	87.9 \pm 2.8	0.92	79.3 \pm 3.4	0.79	87.9 \pm 2.8	0.94	80.7 \pm 3.3	0.84
Filter 20%	92.1 \pm 2.3	0.96	91.4 \pm 2.4	0.94	93.6 \pm 2.1	0.97	90.7 \pm 2.5	0.95
Filter 30%	95 \pm 1.8	0.97	96.4 \pm 1.6	0.98	95.7 \pm 1.7	0.99	92.9 \pm 2.2	0.94
Filter 40%	92.1 \pm 2.3	0.97	89.3 \pm 2.6	0.89	94.3 \pm 1.9	0.97	90.7 \pm 2.5	0.89
Filter 50%	85.7 \pm 2.9	0.93	82.9 \pm 3.2	0.83	87.9 \pm 2.8	0.97	85.7 \pm 3	0.91

It can be observed that the classification performance from all classifiers is improved when the filtering process is applied. Table 1 and Table 3 show that the optimal filtering level for persistent images and entropy features in the MIAS dataset is at filter 20%. NN, DT, and KNN attain an accuracy of 92.3% for both topological features with an AUC value of 0.9 and above. For the DDSM dataset in Tables 2 and 4, filter 30% delivered remarkable results, with all classifiers achieving above 92.9% accuracy and up to 0.99 AUC. Note that, the performance in the DDSM database is more consistent in all classifiers since we utilised more images (140 images) than MIAS, which only used 26 images.

The classification performance can be significantly improved by concatenating features (multi-vector). For example, in MIAS dataset, the performance is improved from 92.3% to 96.2% accuracy and increased up to 99.3% in the DDSM dataset, as shown in Tables 5 and 6.

Table 5. Classification performance of concatenating features in MIAS dataset

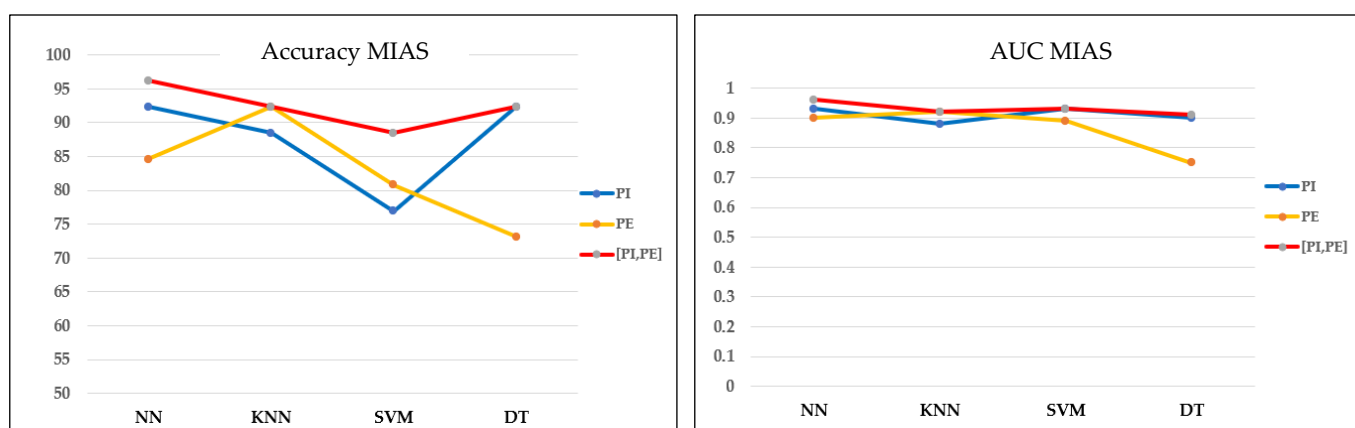
Concatenate Features	NN		KNN		SVM		DT	
	CA \pm Std	AUC	CA \pm Std	AUC	CA \pm Std	AUC	CA \pm Std	AUC
No Filter	61.5 \pm 9.5	0.6	53.8 \pm 9.8	0.54	69.2 \pm 9.1	0.82	69.2 \pm 9.1	0.68
Filter 10%	61.5 \pm 9.5	0.67	53.8 \pm 9.8	0.54	69.2 \pm 9.1	0.79	73.1 \pm 8.7	0.74
Filter 20%	96.2 \pm 3.7	0.96	92.3 \pm 5.2	0.92	88.5 \pm 6.3	0.93	92.3 \pm 5.2	0.91
Filter 30%	84.6 \pm 7.1	0.84	80.8 \pm 7.7	0.81	80.8 \pm 7.7	0.89	84.6 \pm 7.1	0.82
Filter 40%	84.6 \pm 7.1	0.83	80.8 \pm 7.7	0.81	80.8 \pm 7.7	0.89	84.6 \pm 7.1	0.77
Filter 50%	76.9 \pm 8.3	0.81	80.8 \pm 7.7	0.81	80.8 \pm 7.7	0.89	84.6 \pm 7.1	0.8

Table 6. Classification performance of concatenate features in DDSM dataset

Concatenate Features	NN		KNN		SVM		DT	
	CA \pm Std	AUC	CA \pm Std	AUC	CA \pm Std	AUC	CA \pm Std	AUC
No Filter	71.4 \pm 3.8	0.75	73.6 \pm 3.7	0.79	75 \pm 3.7	0.81	68.6 \pm 3.9	0.73
Filter 10%	90 \pm 2.5	0.95	90 \pm 2.5	0.9	91.4 \pm 2.4	0.96	90 \pm 2.5	0.91
Filter 20%	94.3 \pm 1.9	0.95	94.3 \pm 1.9	0.94	97.1 \pm 1.4	0.99	92.9 \pm 2.2	0.93
Filter 30%	97.9 \pm 1.2	0.98	99.3 \pm 0.7	0.99	98.6 \pm 1	0.99	97.9 \pm 1.2	0.98
Filter 40%	92.9 \pm 2.2	0.95	92.1 \pm 2.3	0.91	95 \pm 1.8	0.99	96.4 \pm 1.6	0.95
Filter 50%	91.4 \pm 2.4	0.94	87.9 \pm 2.8	0.88	87.9 \pm 2.8	0.97	87.9 \pm 2.7	0.9

3.3 Performance of Machine Learning Models

Based on the optimal filtering level in both datasets, the performances of four classifiers were evaluated and compared in terms of accuracy, the AUC, and the confusion matrix. Referring to the MIAS dataset in Figure 10, most models obtain good performance on concatenate features with more than 0.9 AUC and a maximum of three misclassified cases in the confusion matrix. Moreover, the accuracy obtained is more than 90%, except for the SVM model. Since this dataset contains three different types of densities, particularly when the breast density is high, the microcalcifications could be obscured by the dense tissues, making it more challenging to classify them. These findings align with the results reported by [50], where the SVM accuracy drops because of the greyscale image's brightness. On the other hand, NN showed the best performance model for this dataset, with the highest accuracy, AUC, and only one false negative case in the confusion matrix.



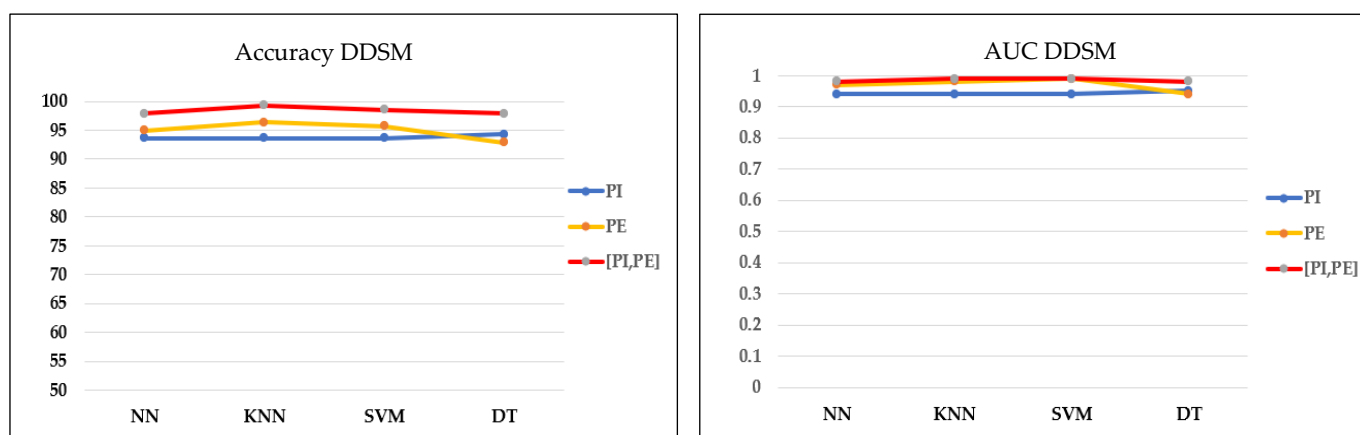
a) Accuracy and AUC of classifiers

Neural Network				KNN				Decision Tree				SVM			
TC	PC			TC	PC			TC	PC			TC	PC		
	Benign	Malignant			Benign	Malignant			Benign	Malignant			Benign	Malignant	
Benign	12	1		Benign	11	2		Benign	12	1		Benign	12	2	
Malignant	0	13		Malignant	0	13		Malignant	1	12		Malignant	1	11	

b) Confusion matrix of concatenating features

Figure 10. Performance comparison of machine learning classifier based on the optimal filter (20%) in the MIAS dataset. TC = True class, PC = Predicted class

In contrast, all models in the DDSM dataset exhibit outstanding classification performance on concatenate features, with more than 95% accuracy, more than 0.97 AUC, and a maximum of three misclassified cases in the confusion matrix, as shown in Figure 11. KNN model performed the best in this dataset with the highest accuracy and only one false negative result.



a) Accuracy and AUC of classifiers

KNN				SVM				Neural Network				Decision Tree			
TC	PC			TC	PC			TC	PC			TC	PC		
	Benign	Malignant			Benign	Malignant			Benign	Malignant			Benign	Malignant	
Benign	69	1		Benign	68	2		Benign	68	2		Benign	69	1	
Malignant	0	70		Malignant	0	70		Malignant	1	69		Malignant	2	68	

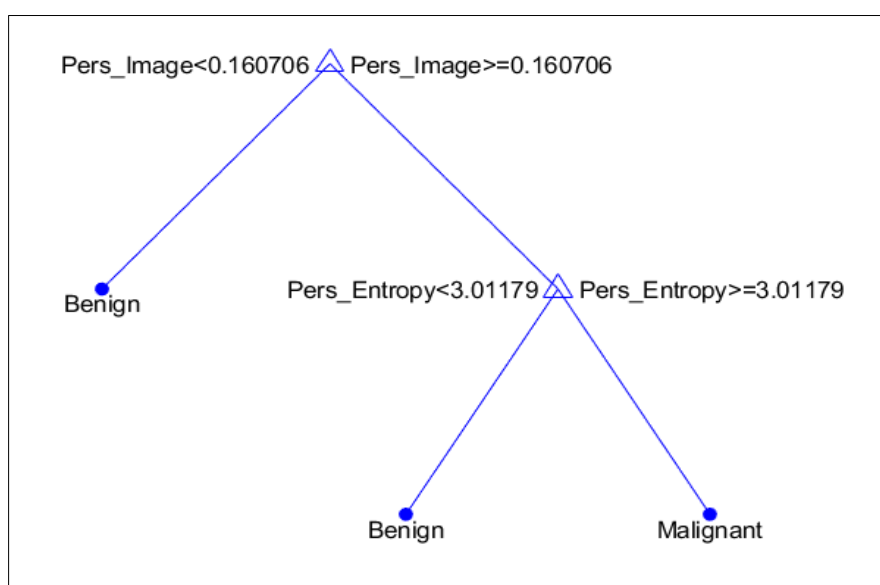
b) Confusion matrix of concatenating features

Figure 11. Performance comparison of machine learning classifier based on the optimal filter (30%) in the DDSM dataset

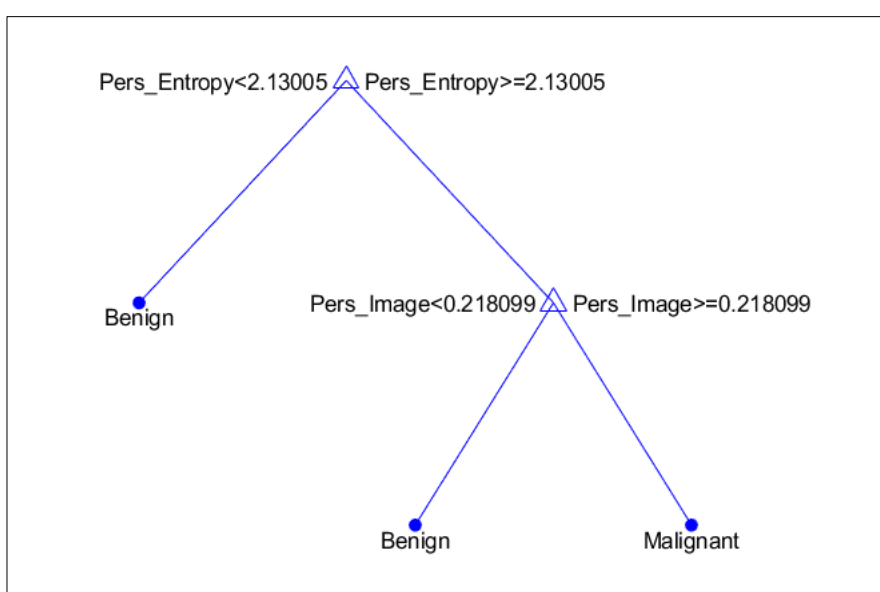
4. Discussion and Future Work

PH is commonly described in the literature as robust against image noise [22,33]. This study demonstrates that if the persistent diagram is taken directly without any filtering on the diagram, machine learning models are unable to classify the vectorised topological features of microcalcification successfully. Experimental results indicate that the performance was improved by implementing the optimal filtering level for each dataset.

It is discovered that, in terms of topological features, PI is more prominent in the MIAS dataset, whereas PE in the DDSM dataset. Figure 12 illustrates the discriminant values of every feature based on the DT model. Compared to malignant microcalcifications, benign microcalcifications will have a lower value of persistent image and entropy.



a) MIAS Dataset



b) DDSM Dataset

Figure 12. Discriminant features values based on the Decision tree model.

In Figure 13, we present some examples of the images from both datasets where benign images have higher values (persistent image and persistent entropy) in non-filter topological features than malignant ones. This result in misclassification between two classes and impact the classification performance. Since benign microcalcifications present a long lifespan in the persistent diagram (refer to Figure 5), the significant topological features can be distinguished after filtering on PD.

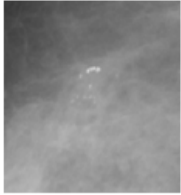
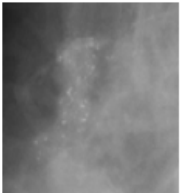
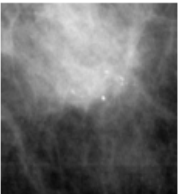
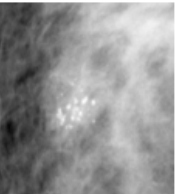
Dataset	Image/Diagnosis	Concatenate Fatures [Persistent Entropy, Persistent Image]					
		Non Filter	10%	20%	30%	40%	50%
MIAS	 Benign	[6.466917160, 1.02027]	[2.9668169, 0.203]	[2.9668169, 0.13743]	[1.314512, 0.08688]	[1.039665, 0.07304]	[0.6387773, 0.0556498]
	 Malignant	[5.460671096, 0.56048]	[3.8144293, 0.28944]	[3.8144293, 0.1953]	[2.418626, 0.94563]	[1.898763, 0.09141]	[1.0625414, 0.0501371]
DDSM	 Benign	[7.042784054, 2.487257776]	[4.5397428, 0.6671438]	[2.6954403, 0.2188888]	[1.844852, 0.1340691]	[0.673671, 0.066563]	[0.673671, 0.0665633]
	 Malignant	[6.488948871, 1.861700577]	[4.5919309, 0.8254817]	[3.520727, 0.4600087]	[2.818247, 0.3041271]	[2.433522, 0.2381287]	[1.5852037, 0.13284499]

Figure 13. Examples of images with topological feature values.

The benefit of using PH is that it represents a less computational burden to the system because the classification operation is not on the image matrix but on a compact vector than the input data [31]. In our case, we utilise only two topological features for each image: persistent entropy and persistent image features, since the complexity of a CAD system increases rapidly with the number of features used [51]. Besides, the proposed filtering procedure does not influence the image quality since the process only operates on the persistent diagram rather than some preprocessing methods, such as linear filtering, which can cause degradation of edges and image details, giving the images a blurring effect[15].

Several existing state-of-the-art for non-PH models that conduct experiments with the same MIAS and DDSM datasets are chosen for performance comparison, as shown in Table 7. Based on this table, two types of images are applied for both datasets: greyscale and binary images. Greyscale indicates that the classification process is performed straight from the original image obtained from the dataset, consisting of 256-pixel values. Meanwhile, the classification of binary images indicates that the original images undergo a segmentation process to produce a black-and-white image where the pixel values of 0 (black) are considered as the background region and pixel values of 1 (white) are considered as segmented regions of microcalcifications. However, some microcalcifications, usually malignant cases, are not clearly visible and closely connected to background tissue, making it impossible for segmentation algorithms to obtain complete segmentation for these calcifications [52]. For that reason, we test our proposed methods for the greyscale images so that the whole topological structure of the image can be considered.

Table 7. Comparative analysis with other methods

Method	Features	Image Type	Dataset	Classifier	Result
Fadil [13]	Texture (DWT and GLCM)	Greyscale	DDSM	RF	CA=95%, AUC = 0.92
Suhail et al. [53]	Local Features	Binary	DDSM	LDA-SVM	CA=96%, AUC = 0.95
Chen et al. [12]	Multiscale Morphology Graph	Binary	MIAS	KNN	CA=95%, AUC = 0.96
			DDSM	KNN	CA=85.2%, AUC = 0.90
Strange et al. [54]	Mereotopological Barcode	Binary	MIAS	KNN	CA=95% , AUC=0.96
			DDSM	KNN	CA=80%, AUC=0.82
Proposed Approach	Persistent Image and Persistent Entropy Features on FPD	Greyscale	MIAS	NN	CA=96.2% , AUC=0.96
			DDSM	KNN	CA=99.3%, AUC=0.99

Research by [13] employed a greyscale image similar to our data type but differed in preprocessing and feature selection steps. They used 2D discrete wavelet transform for contrast enhancement of the microcalcifications and extracted eight textural features on the grey level cooccurrence matrix (GLCM), achieving 95% accuracy and 0.92 AUC. In work related to extracting features on the segmented image (binary type), Suhail et al. [53] present a way to get a single feature value by applying a scalable Linear Fisher Discriminant Analysis (LDA) approach achieved up to 96% accuracy with 0.95 AUC. In addition, the topological approach has also been studied by [12,54] for modelling and classification of microcalcifications with promising results. To our knowledge, our proposed method is the first work using a persistent diagram as a filtering approach to tackle the challenge of discriminant between benign and malignant microcalcifications. Our method achieves 96.2% accuracy with 0.96 AUC for the MIAS dataset and 99.3% accuracy with 0.99 AUC for the DDSM dataset. This is comparable with other state-of-the-art non-PH approaches developed to solve the same problem.

Although the performance is satisfactory, additional testing must be conducted on mammographic images collected from hospitals or population screening projects. In addition, increasing the number of cases with breast microcalcifications would permit a more in-depth assessment of the suggested method and make it easier to determine the ideal diagnostic performance of our model and its potential value in future applications.

5. Conclusions

In conclusion, this study presents an approach to classifying microcalcifications in mammogram images using Persistent Homology and machine learning models. This study demonstrates that machine learning models can successfully classify microcalcifications using appropriate PH filtering levels and features. We also discover that filtering PD with concatenate features improves the classification accuracy of microcalcifications. The results are significant, and we hope it will support radiologists in making the right decisions and preventing unnecessary biopsies.

Author Contributions: Conceptualisation, A.A.M and M.S.M.N; methodology, A.A.M, M.A.A, M.S.M.N, F.A.A; software, A.A.M; validation, all authors; formal analysis, A.A.M; data curation, A.A.M; writing—original draft preparation, A.A.M; writing—review and editing, all authors; visualisation, A.A.M; supervision, M.A.A, M.S.M.N, F.A.A; funding acquisition, M.A.A and F.A.A. All authors have read and agreed to the published version of the manuscript.

Funding: This work was supported by the Universiti Kebangsaan Malaysia (UKM) for Internal grant GUP-2021-046 and Tabung Agihan Penyelidikan (TAP)(grant number TAP-K020061).

Institutional Review Board Statement: There are no ethical implications on the public datasets.

Informed Consent Statement: Patient consent was waived due to the implementation in public datasets.

Data Availability Statement: The public datasets are available in the publicly accessible repository; refer [7] for MIAS and [38] for DDSM datasets.

Acknowledgments: M.A.A gratefully acknowledges Universiti Kebangsaan Malaysia for Internal grant and Tabung Agihan Pendapatan (TAP) without which the research would not have been possible. A.A.M is thankful to the Ministry of Higher Education (MOHE) of Malaysia and Universiti Teknologi MARA (UiTM) for the full scholarship (SLAB). The authors would like to thank the anonymous referees for their expert advice and suggestions, which helped to improve this paper.

Conflicts of Interest: The authors declare no conflict of interest.

References

1. Ferlay, J.; Colombet, M.; Soerjomataram, I.; Parkin, D.M.; Piñeros, M.; Znaor, A.; Bray, F. Cancer Statistics for the Year 2020: An Overview. *Int J Cancer* **2021**, doi:10.1002/ijc.33588.
2. Vy, V.P.T.; Yao, M.M.-S.; Le, N.Q.K.; Chan, W.P. Machine Learning Algorithm for Distinguishing Ductal Carcinoma in Situ from Invasive Breast Cancer. *Cancers (Basel)* **2022**, *14*, doi:10.3390/cancers14102437.
3. Ramadan, S.Z. Methods Used in Computer-Aided Diagnosis for Breast Cancer Detection Using Mammograms: A Review. *J Healthc Eng* **2020**, *2020*, doi:10.1155/2020/9162464.
4. Htay, M.N.N.; Donnelly, M.; Schliemann, D.; Loh, S.Y.; Dahlui, M.; Somasundaram, S.; Tamin, N.S.B.I.; Su, T.T. Breast Cancer Screening in Malaysia: A Policy Review. *Asian Pac J Cancer Prev* **2021**, *22*, 1685, doi:10.31557/APJCP.2021.22.6.1685.
5. Melekoodappattu, J.G.; Subbian, P.S.; Queen, M.P.F. Detection and Classification of Breast Cancer from Digital Mammograms Using Hybrid Extreme Learning Machine Classifier. *Int J Imaging Syst Technol* **2021**, *31*, 909–920, doi:10.1002/ima.22484.
6. Oliver, A.; Torrent, A.; Lladó, X.; Tortajada, M.; Tortajada, L.; Sentís, M.; Freixenet, J.; Zwigglelaar, R. Automatic Microcalcification and Cluster Detection for Digital and Digitised Mammograms. *Knowl Based Syst* **2012**, *28*, 68–75, doi:10.1016/j.knosys.2011.11.021.
7. Suckling, J. The Mammographic Image Analysis Society Digital Mammogram Database. *Excerpta Medica International Congress* **1994**, 375–386.
8. Azam, A.S.B.; Malek, A.A.; Ramlee, A.S.; Suhaimi, N.D.S.M.; Mohamed, N. Segmentation of Breast Microcalcification Using Hybrid Method of Canny Algorithm with Otsu Thresholding and 2D Wavelet Transform. In Proceedings of the 2020 10th IEEE International Conference on Control System, Computing and Engineering (ICCSCE); 2020; pp. 91–96.
9. Dabass, J.; Arora, S.; Vig, R.; Hanmandlu, M. Segmentation Techniques for Breast Cancer Imaging Modalities-A Review. In Proceedings of the 2019 9th International Conference on Cloud Computing, Data Science & Engineering (Confluence); 2019; pp. 658–663.

10. Banumathy, D.; Khalaf, O.I.; Romero, C.A.T.; Raja, P. v; Sharma, D.K. Breast Calcifications and Histopathological Analysis on Tumour Detection by CNN. *Computer Systems Science and Engineering* **2023**, *44*, 595–612, doi:10.32604/csse.2023.025611. 704
11. Roty, S.; Wiratkapun, C.; Tanawongsuwan, R.; Phongsuphap, S. Analysis of Microcalcification Features for Pathological Classification of Mammograms. In Proceedings of the 2017 10th Biomedical Engineering International Conference (BMEiCON); 2017; pp. 1–5. 705
12. Chen, Z.; Strange, H.; Oliver, A.; Denton, E.R.E.; Boggis, C.; Zwigelaar, R. Topological Modeling and Classification of Mammographic Microcalcification Clusters. *IEEE Trans Biomed Eng* **2015**, *62*, 1203–1214, doi:10.1109/TBME.2014.2385102. 706
13. Fadil, R.; Jackson, A.; el Majd, B.A.; el Ghazi, H.; Kaabouch, N. Classification of Microcalcifications in Mammograms Using 2D Discrete Wavelet Transform and Random Forest. In Proceedings of the 2020 IEEE International Conference on Electro Information Technology (EIT); 2020; pp. 353–359. 707
14. Fan, L.; Zhang, F.; Fan, H.; Zhang, C. Brief Review of Image Denoising Techniques. *Vis Comput Ind Biomed Art* **2019**, *2*, 7, doi:10.1186/s42492-019-0016-7. 708
15. Krishnan, A. An Overview Of Mammogram Noise And Denoising Techniques. *International Journal of Engineering Research and General Science* **2016**, *4*, 557–563. 709
16. Patil, R.S.; Biradar, N. Automated Mammogram Breast Cancer Detection Using the Optimized Combination of Convolutional and Recurrent Neural Network. *Evol Intell* **2020**, *14*, 1459–1474, doi:10.1007/s12065-020-00403-x. 710
17. Kshema; George, M.J.; Dhas, D.A.S. Preprocessing Filters for Mammogram Images: A Review. In Proceedings of the 2017 Conference on Emerging Devices and Smart Systems (ICEDSS); 2017; pp. 1–7. 711
18. Hamed, G.; Marey, M.; Amin, S.E.-S.; Tolba, M.F. A Proposed Model for Denoising Breast Mammogram Images. In Proceedings of the 2018 13th International Conference on Computer Engineering and Systems (ICCES); 2018; pp. 652–657. 712
19. Mahmood, T.; Li, J.; Pei, Y.; Akhtar, F.; Imran, A.; Yaqub, M. An Automatic Detection and Localization of Mammographic Microcalcifications ROI with Multi-Scale Features Using the Radiomics Analysis Approach. *Cancers (Basel)* **2021**, *13*. 713
20. Loizidou, K.; Skouroumouni, G.; Pitris, C.; Nikolaou, C. Digital Subtraction of Temporally Sequential Mammograms for Improved Detection and Classification of Microcalcifications. *Eur Radiol Exp* **2021**, *5*, doi:10.1186/s41747-021-00238-w. 714
21. Pun, C.S.; Lee, S.X.; Xia, K. Persistent-Homology-Based Machine Learning: A Survey and a Comparative Study. *Artif Intell Rev* **2022**, *55*, 5169–5213, doi:10.1007/s10462-022-10146-z. 715
22. Conti, F.; Moroni, D.; Pascali, M.A. A Topological Machine Learning Pipeline for Classification. *Mathematics* **2022**, *10*. 716
23. Nishio, M.; Nishio, M.; Jimbo, N.; Nakane, K. Homology-Based Image Processing for Automatic Classification of Histopathological Images of Lung Tissue. *Cancers (Basel)* **2021**, *13*, 1–12, doi:10.3390/cancers13061192. 717
24. Carlsson, G. Topology and Data. *Bulletin of the American Mathematical Society* **2009**, *46*, 255–308. 718
25. Choe, S.; Ramanna, S. Cubical Homology-Based Machine Learning: An Application in Image Classification. *Axioms* **2022**, *11*, doi:10.3390/axioms11030112. 719
26. Asaad, A.; Jassim, S. Topological Data Analysis for Image Tampering Detection Aras. In Proceedings of the Lecture Notes in Computer Science; Springer Cham, 2017; Vol. 10431, pp. 136–146. 720

27. Asaad, A.; Ali, D.; Majeed, T.; Rashid, R. Persistent Homology for Breast Tumor Classification Using Mammogram Scans. *Mathematics* **2022**, *10*. 746 747
28. Kusano, G.; Fukumizu, K.; Hiraoka, Y. Kernel Method for Persistence Diagrams via Kernel Embedding and Weight Factor. *Journal of Machine Learning Research* **2018**, *18*, 1–41. 748 749
29. Moroni, D.; Pascali, M.A. Learning Topology: Bridging Computational Topology and Machine Learning. *Pattern Recognition and Image Analysis* **2021**, *31*, 443–453, doi:10.1134/S1054661821030184. 750 751
30. Chazal, F.; Fasy, B.; Lecci, F.; Michel, B.; Rinaldo, A.; Wasserman, L. Robust Topological Inference: Distance to a Measure and Kernel Distance. *Journal of Machine Learning Research* **2018**, *18*, 1–40. 752 753
31. Avilés-Rodríguez, G.J.; Nieto-Hipólito, J.I.; Cosío-León, M.D.L.Á.; Romo-Cárdenas, G.S.; Sánchez-López, J.D.D.; Radilla-Chávez, P.; Vázquez-Briseño, M. Topological Data Analysis for Eye Fundus Image Quality Assessment. *Diagnostics* **2021**, *11*, doi:10.3390/diagnostics11081322. 754 755 756
32. Adams, H.; Emerson, T.; Kirby, M.; Neville, R.; Peterson, C.; Shipman, P.; Chepushtanova, S.; Hanson, E.; Motta, F.; Ziegelmeier, L. Persistence Images: A Stable Vector Representation of Persistent Homology. *Journal of Machine Learning Research* **2017**, *18*, 1–35. 757 758 759
33. Teramoto, T.; Shinohara, T.; Takiyama, A. Computer-Aided Classification of Hepatocellular Ballooning in Liver Biopsies from Patients with NASH Using Persistent Homology. *Comput Methods Programs Biomed* **2020**, *195*, doi:10.1016/j.cmpb.2020.105614. 760 761 762
34. Oyama, A.; Hiraoka, Y.; Obayashi, I.; Saikawa, Y.; Furui, S.; Shiraishi, K.; Kumagai, S.; Hayashi, T.; Kotoku, J. Hepatic Tumor Classification Using Texture and Topology Analysis of Non-Contrast-Enhanced Three-Dimensional T1-Weighted MR Images with a Radiomics Approach. *Sci Rep* **2019**, *9*, 2–11, doi:10.1038/s41598-019-45283-z. 763 764 765 766
35. Leykam, D.; Rondón, I.; Angelakis, D.G. Dark Soliton Detection Using Persistent Homology. *Chaos: An Interdisciplinary Journal of Nonlinear Science* **2022**, *32*, 73133, doi:10.1063/5.0097053. 767 768
36. Edwards, P.; Skruber, K.; Milićević, N.; Heidings, J.B.; Read, T.A.; Bubenik, P.; Vitriol, E.A. TDAExplore: Quantitative Analysis of Fluorescence Microscopy Images through Topology-Based Machine Learning. *Patterns* **2021**, *2*, doi:10.1016/j.patter.2021.100367. 769 770 771
37. Rammal, A.; Assaf, R.; Goupil, A.; Kacim, M.; Vrabie, V. Machine Learning Techniques on Homological Persistence Features for Prostate Cancer Diagnosis. *BMC Bioinformatics* **2022**, *23*, 1–22, doi:10.1186/s12859-022-04992-5. 772 773 774
38. Heath, M.; Bowyer, K.; Kopans, D.; Moore, R.; Kegelmeyer, P. The Digital Database for Screening Mammography. In Proceedings of the Fifth International Workshop on Digital Mammography; 2000; pp. 212–218. 775 776 777
39. Beksi, W.J.; Papanikolopoulos, N. 3D Region Segmentation Using Topological Persistence. In Proceedings of the 2016 IEEE/RSJ International Conference on Intelligent Robots and Systems (IROS); 2016; pp. 1079–1084. 778 779 780
40. Leykam, D.; Rondon, I.; Angelakis, D.G. Dark Soliton Detection Using Persistent Homology. *arXiv:2107.14594 [physics, physics:quant-ph]* **2021**, 073133, doi:10.1063/5.0097053. 781 782
41. Otter, N.; Porter, M.A.; Tillmann, U.; Grindrod, P.; Harrington, H.A. A Roadmap for the Computation of Persistent Homology. *EPJ Data Sci* **2017**, *6*, 1–38. 783 784
42. Kramár, M.; Levanger, R.; Tithof, J.; Suri, B.; Xu, M.; Paul, M.; Schatz, M.F.; Mischaikow, K. Analysis of Kolmogorov Flow and Rayleigh–Bénard Convection Using Persistent Homology. *Physica D* **2016**, *334*, 82–98, doi:10.1016/j.physd.2016.02.003. 785 786 787

43. Garin, A.; Tauzin, G. A Topological “reading” Lesson: Classification of MNIST Using TDA. *Proceedings - 18th IEEE International Conference on Machine Learning and Applications, ICMLA 2019* **2019**, 1551–1556, doi:10.1109/ICMLA.2019.00256. 788
789
44. Pun, C.S.; Xia, K.; Lee, S.X. Persistent-Homology-Based Machine Learning and Its Applications--A Survey. *arXiv preprint arXiv:1811.00252* **2018**. 790
791
45. Chazal, F.; Michel, B. An Introduction to Topological Data Analysis: Fundamental and Practical Aspects for Data Scientists. *Front Artif Intell* **2021**, *4*, 1–28, doi:10.3389/frai.2021.667963. 792
793
46. Atienza, N.; Gonzalez-Díaz, R.; Soriano-Trigueros, M. On the Stability of Persistent Entropy and New Summary Functions for Topological Data Analysis. *Pattern Recognit* **2020**, *107*, 107509, doi:10.1016/j.patcog.2020.107509. 794
795
796
797
47. Moon, C.; Li, Q.; Xiao, G. Using Persistent Homology Topological Features to Characterize Medical Images: Case Studies on Lung and Brain Cancers. *arXiv preprint arXiv:2012.12102* **2020**. 798
799
48. Kaji, S.; Sudo, T.; Ahara, K. Cubical Ripser: Software for Computing Persistent Homology of Image and Volume Data. **2020**, *D*, 1–9. 800
801
49. Jiao, Y.; Du, P. Performance Measures in Evaluating Machine Learning Based Bioinformatics Predictors for Classifications. *Quantitative Biology* **2016**, *4*, 320–330, doi:10.1007/s40484-016-0081-2. 802
803
50. Turkes, R.; Nys, J.; Verdonck, T.; Latre, S. Noise Robustness of Persistent Homology on Greyscale Images, across Filtrations and Signatures. *PLoS One* **2021**, *16*, 1–26, doi:10.1371/journal.pone.0257215. 804
805
51. Sakka, E.; Prentza, A.; Koutsouris, D. Classification Algorithms for Microcalcifications in Mammograms (Review). *Oncol Rep* **2006**, *15*, 1049–1055. 806
807
52. Temmermans, F.; Jansen, B.; Willekens, I.; van de Castele, E.; Deklerck, R.; Schelkens, P.; de Mey, J. Classification of Microcalcifications Using Micro-CT. In *Proceedings of the Applications of Digital Image Processing XXXVI*; Tescher, A.G., Ed.; 2013; Vol. 8856. 808
809
810
53. Suhail, Z.; Denton, E.R.E.; Zwigelaar, R. Classification of Micro-Calcification in Mammograms Using Scalable Linear Fisher Discriminant Analysis. *Med Biol Eng Comput* **2018**, *56*, 1475–1485, doi:10.1007/s11517-017-1774-z. 811
812
813
54. Strange, H.; Chen, Z.; Denton, E.R.E.; Zwigelaar, R. Modelling Mammographic Microcalcification Clusters Using Persistent Mereotopology. *Pattern Recognit Lett* **2014**, *47*, 157–163, doi:10.1016/j.patrec.2014.04.008. 814
815
816
817